

Preferential Destruction of Micropollutants in Water through a Self-Purification Process with Dissolved Organic Carbon Polar Complexation

Yumeng Wang, Peng Zhang, Lai Lyu, Tong Li, and Chun Hu*



Cite This: *Environ. Sci. Technol.* 2022, 56, 10849–10856



Read Online

ACCESS |

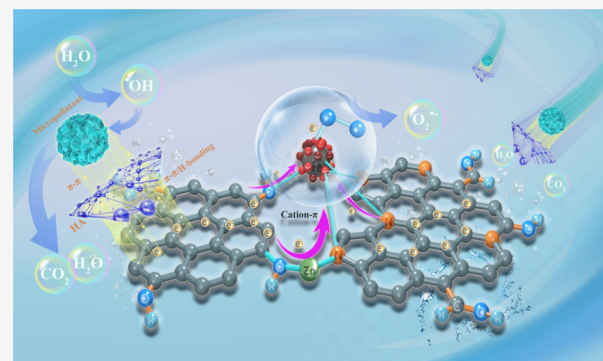
Metrics & More

Article Recommendations

Supporting Information

ABSTRACT: Removing micropollutants in real water is a scientific challenge due to primary dissolved organic carbon (DOC) and high energy consumption of current technologies. Herein, we develop a self-purification process for the preferential destruction of various micropollutants in municipal wastewater, raw drinking water, and ultrapure water with humic acid (HA) driven by the surface microelectronic field of $\text{Fe}^0\text{-Fe}_y\text{C}_z/\text{Fe}_x\text{-GZIF-8-rGO}$ without any additional input. It was verified that a strongly polar complex consisting of an electron-rich HA/DOC area and an electron-poor micropollutant area was formed between HA/DOC and micropollutants, promoting more electrons of micropollutants in the adsorbed complex to delocalizing to electron-rich Fe species area and be trapped by O_2 , which resulted in their surface cleavage and hydrolyzation preferentially. The higher micropollutant degradation efficiency observed in real wastewaters was due to the greater complex polarity of DOC. Moreover, the electron transfer process ensured the stability of the surface microelectronic field and continuous water purification. Our findings provide a new insight into low-energy combined-micropollution water treatment.

KEYWORDS: micropollutant, preferential destruction, dissolved organic carbon, polar complexation, self-purification



INTRODUCTION

The increasing complex-mixture micropollution in aquatic systems with thousands of industrial chemical compounds has received great attention due to its potential to cause undesirable effects on aquatic life and human health.¹ Especially, pesticides, pharmaceuticals, personal care products, endocrine disrupting chemicals, and so on were widely detected in municipal wastewater, raw drinking water, and reclaimed wastewater, with the trace levels ranging from ng/L to $\mu\text{g}/\text{L}$,^{2–4} even in filtered water and tap water.^{5,6} Therefore, removing these micropollutants from water is very important and urgent to avoid long-term human and biological exposure.

Over the past few decades, a wide range of advanced treatment methods has been investigated for the removal of micropollutants from different waters. For drinking-water treatment, physical methods including adsorption and membrane filtration could mitigate micropollutants available by 15–95 and 70–98%, respectively,⁷ due to the interference of primary dissolved organic carbon (DOC).^{1,8} To remove micropollutants from large quantities of raw drinking water, municipal wastewater, and reclaimed wastewater, these processes often require the assistance of reactive oxidants.^{9–11} However, complete removal is still not feasible (9–99%)^{7,12} due to the competition of mg-level DOC in water for oxidants.¹³

Recently, the advanced oxidation process (AOP) has been widely considered the most promising method for water purification, which could completely remove various micropollutants from synthetic wastewater in the laboratory^{14,15} but not in real wastewaters. However, it is still a great scientific challenge to perform preferential removal of these toxic refractory micropollutants at the trace level from real water due to the competition of coexisting DOC and other compounds.^{16,17} In municipal wastewater and raw drinking water, natural organic matter (NOM) occupies 50–90% of the DOC, being mainly composed of humic acid (HA). It was found that HA is a heterogeneous, redox-active organic macromolecule with an electron-rich semiquinone radical, in which the phenolic $-\text{OH}$ group is the electron-donating moiety, while the benzoquinone group is the electron-accepting moiety.¹⁸ Moreover, HA was also able to aggregate abiotically to a complex in a natural water environment,

Received: May 10, 2022

Revised: July 12, 2022

Accepted: July 12, 2022

Published: July 21, 2022



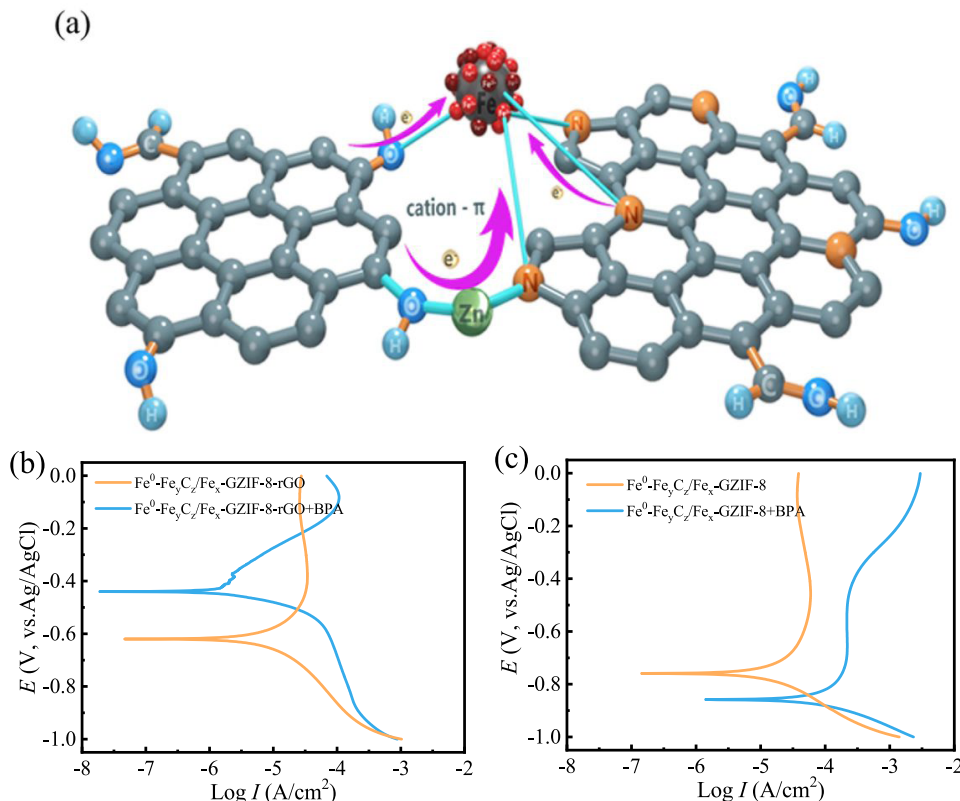


Figure 1. (a) Configuration of $\text{Fe}^0\text{-Fe}_y\text{C}_z/\text{Fe}_x\text{-GZIF-8-rGO}$. Tafel plots of (b) $\text{Fe}^0\text{-Fe}_y\text{C}_z/\text{Fe}_x\text{-GZIF-8-rGO}$ and (c) $\text{Fe}^0\text{-Fe}_y\text{C}_z/\text{Fe}_x\text{-GZIF-8}$ before and after the reaction with BPA.

promoting its utilization by planktonic bacterivores,¹⁹ suggesting that the formed particles may have greater electron polarity than HA. Therefore, investigating the interaction mode between the self-organized complex and micropollutants may be key to developing technologies for the preferential removal of micropollutants.

Recently, we developed a novel catalyst ($\text{Fe}^0\text{-Fe}_y\text{C}_z/\text{Fe}_x\text{-GZIF-8-rGO}$) consisting of $\text{Fe}^0\text{-Fe}_y\text{C}_z/\text{Fe}_x$, graphited ZIF-8 (GZIF-8), and reduced graphene oxide (rGO) with three chemical coordination bonds at the interface of different phases, including Fe–O–C between $\text{Fe}^0\text{-Fe}_y\text{C}_z/\text{Fe}_x$ and rGO, Fe–N between $\text{Fe}^0\text{-Fe}_y\text{C}_z/\text{Fe}_x$ and GZIF-8, and C–O–Zn–N between GZIF-8 and rGO. Thus, on the catalyst surface, a strong $\text{Fe}(\text{Zn})-\pi$ electrostatic interaction occurred, resulting in the electron-rich area around the Fe species and the electron-poor area around the aromatic rings of GZIF-8 and rGO.^{20,21} By the strong surface electrostatic force, most of the refractory organic pollutants in ultrapure water were almost completely destroyed and mineralized without additional energy through their surface complexation and cleavage, meanwhile converting H_2O to $\cdot\text{OH}$ for water purification. Our findings indicate that both complexation and cleavage of reactants on the catalyst surface were crucial to driving the water-purification reaction for the developed technology. Therefore, the form of DOC in real water and its interaction with micropollutants may be very important factors for the selective elimination of micropollutants in municipal wastewater and raw drinking water.

In the present study, hydrophilic micropollutants such as bisphenol (BPA), 2-chlorophenol (2-CP), ciprofloxacin (CIP), ibuprofen (IBU), and 2,4-dichlorophenoxyacetic acid (2,4-D);

hydrophobic micropollutants such as diphenhydramine (DP); and heterocyclic micropollutants such as atrazine (ATZ) were selected as ubiquitous micropollutants in the aquatic system to investigate their degradation in synthetic wastewater with HA, actual municipal wastewater, and raw drinking water through $\text{Fe}^0\text{-Fe}_y\text{C}_z/\text{Fe}_x\text{-GZIF-8-rGO}$ air-saturated aqueous suspensions. It was found that the tested micropollutants were selectively degraded preferentially, while both HA and DOC from real wastewater enhanced the surface cleavage of the tested micropollutants through their polarized complexation. Furthermore, the complexation and electron polarizing among the pollutants/HA/DOC/catalyst were characterized through Fourier-transform infrared (FTIR), electron paramagnetic resonance (EPR), and density functional theory (DFT) calculation methods. A mechanism was proposed for surface complexes driving the preferential removal of micropollutants in the $\text{Fe}^0\text{-Fe}_y\text{C}_z/\text{Fe}_x\text{-GZIF-8-rGO}$ air-saturated aqueous suspension. Our findings provide a new insight into developing a low-energy purification technology for combined-micro-pollution water.

EXPERIMENTAL SECTION

The details including materials and catalyst synthesis, catalytic tests and analyses, theoretical computation methods, three-dimensional excitation–emission matrix (3D-EEM) fluorescence measurements, detection methods of radicals, FTIR measurements, gas chromatography–mass spectrometry (GC-MS) analysis, and electrochemical measurements are presented in the Supporting Information (SI).

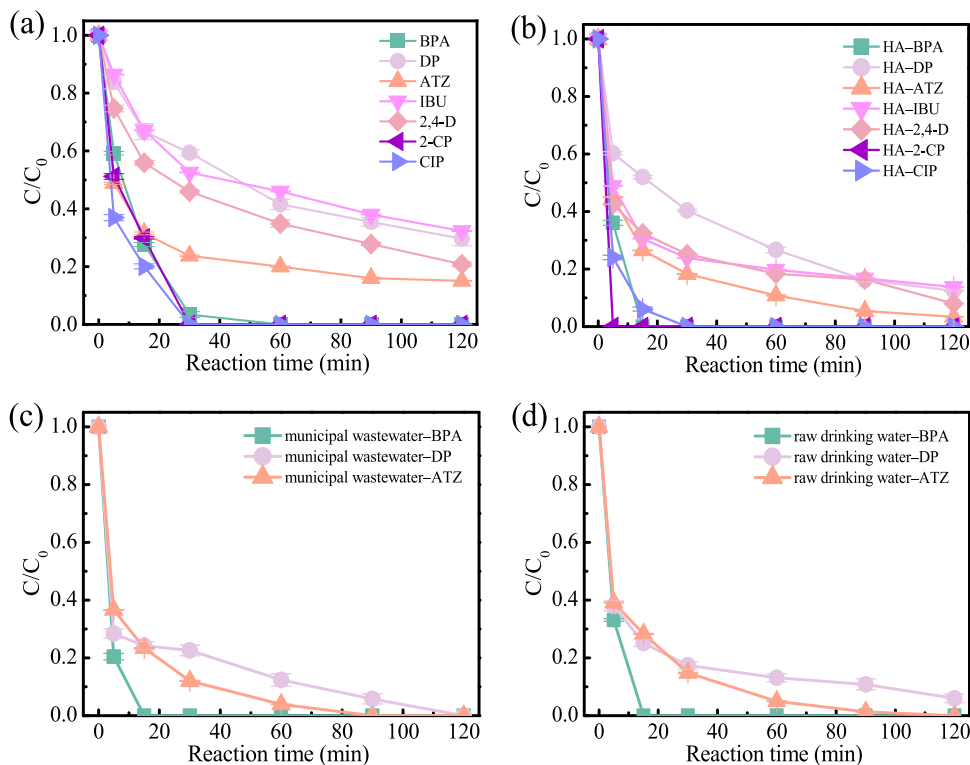


Figure 2. Degradation curves of various micropollutants (a) without HA and (b) with HA in ultrapure water. Degradation curves of BPA, DP, and ATZ in (c) municipal wastewater and (d) raw drinking water suspension. Reaction conditions: catalyst concentration 0.6 g/L, initial micropollutant concentration 3.0 mg/L, initial HA concentration 10.0 mg/L, and temperature 35 °C.

RESULTS AND DISCUSSION

Microelectric Field Stability and Performance of $\text{Fe}^0\text{-Fe}_y\text{C}_z/\text{Fe}_x\text{-GZIF-8-rGO}$. According to previous characterizations,²⁰ on the surface of $\text{Fe}^0\text{-Fe}_y\text{C}_z/\text{Fe}_x\text{-GZIF-8-rGO}$, a strong cation (Fe or Zn)- π interaction occurred with the delocalized π orbitals perpendicular to the plane of the aromatic rings of GZIF-8/rGO from the chemical coordination bonds between surface Fe/Zn species and the aromatic structure (Figure 1a). Based on this configuration, the DFT calculations demonstrated that the electron-rich area was formed around the Fe species and the electron-poor area was formed around the aromatic structure of GZIF-8/rGO, with electrostatic potentials of 61.26–134.77 kcal/mol and -24.11 to -13.03 kcal/mol, respectively (Figure S1).²⁰ Therefore, the surface potential energy produced between both areas could reach 663.96/547.38/310.97 kJ/mol.

It is widely known that Fe^0 corrosion can degrade pollutants. The surface microelectric field stability of $\text{Fe}^0\text{-Fe}_y\text{C}_z/\text{Fe}_x\text{-GZIF-8-rGO}$ was measured by Tafel polarization before and after the reaction with BPA with a reference of unstable $\text{Fe}^0\text{-Fe}_y\text{C}_z/\text{Fe}_x\text{-GZIF-8}$.²⁰ The corrosion current density of $\text{Fe}^0\text{-Fe}_y\text{C}_z/\text{Fe}_x\text{-GZIF-8-rGO}$ was 10.99 $\mu\text{A}/\text{cm}^2$, which decreased to 4.67 $\mu\text{A}/\text{cm}^2$ after reaction with BPA, while the value of $\text{Fe}^0\text{-Fe}_y\text{C}_z/\text{Fe}_x\text{-GZIF-8}$ was 20.82 $\mu\text{A}/\text{cm}^2$, and it significantly increased to 120 $\mu\text{A}/\text{cm}^2$ in the BPA-adsorbed $\text{Fe}^0\text{-Fe}_y\text{C}_z/\text{Fe}_x\text{-GZIF-8}$ sample (Figure 1b,c). Correspondingly, the corrosion potentials of $\text{Fe}^0\text{-Fe}_y\text{C}_z/\text{Fe}_x\text{-GZIF-8-rGO}$ exhibited a positive shift from -0.620 to -0.439 V after the reaction, indicating corrosion inhibition. However, a negative shift (-0.758 → -0.859 V) was observed in the $\text{Fe}^0\text{-Fe}_y\text{C}_z/\text{Fe}_x\text{-GZIF-8}$ sample (Figure 1b,c), indicative of corrosion occurring. The results further confirmed that the electron from BPA was delocalized

to the electron-rich Fe species area due to the (Fe or Zn)- π interaction, which greatly strengthens the microelectric field stability of the catalyst. However, opposite phenomena appeared on $\text{Fe}^0\text{-Fe}_y\text{C}_z/\text{Fe}_x\text{-GZIF-8}$. Moreover, according to our previous research,²⁰ in the N_2 -saturated suspension with Fe^{3+} addition, $\text{Fe}^0\text{-Fe}_y\text{C}_z/\text{Fe}_x\text{-GZIF-8-rGO}$ exhibited the same catalytic activity as that under the air-saturated condition, while no significant oxidation was observed under the N_2 -saturated condition. The results indicated that O_2 mainly served as an electron acceptor for maintaining pollutant degradation. Pollutant degradation mainly depended on the surface cleavage and hydrolysis process on the $\text{Fe}^0\text{-Fe}_y\text{C}_z/\text{Fe}_x\text{-GZIF-8-rGO}$ surface due to strong surface electrostatic forces.

Preferential Removal of Micropollutants in Different Waters Using $\text{Fe}^0\text{-Fe}_y\text{C}_z/\text{Fe}_x\text{-GZIF-8-rGO}$. All of the tested micropollutants (Figure S2) were degraded in different air-saturated waters using $\text{Fe}^0\text{-Fe}_y\text{C}_z/\text{Fe}_x\text{-GZIF-8-rGO}$ (Figure 2). Compared with the $\text{Fe}^0\text{-Fe}_y\text{C}_z/\text{Fe}_x\text{-GZIF-8-rGO}/\text{HA}$ suspension, the $\text{Fe}^0\text{-Fe}_y\text{C}_z/\text{Fe}_x\text{-GZIF-8-rGO}/\text{HA}$ suspension showed a higher degradation efficiency for micropollutants (Figure 2a,b). BPA, 2-CP, and CIP could be completely removed in 5–15 min, and the degradation efficiencies of DP, ATZ, IBU, and 2,4-D increased to 87.6, 96.6, 86.3, and 92.0%, respectively, within 120 min (Figure 2b). Moreover, a much higher efficiency was observed in municipal wastewater and raw drinking water. Almost complete degradation of BPA, DP, and ATZ was achieved within 15, 90, and 120 min, respectively (Figure 2c,d). The phenomena were absolutely different from those in general oxidizing processes, in which DOC predominantly including NOM, such as HA, depressed the degradation of micropollutants.¹⁷ Furthermore, the intermediates from the degradation of DP with HA (HA-DP) in the

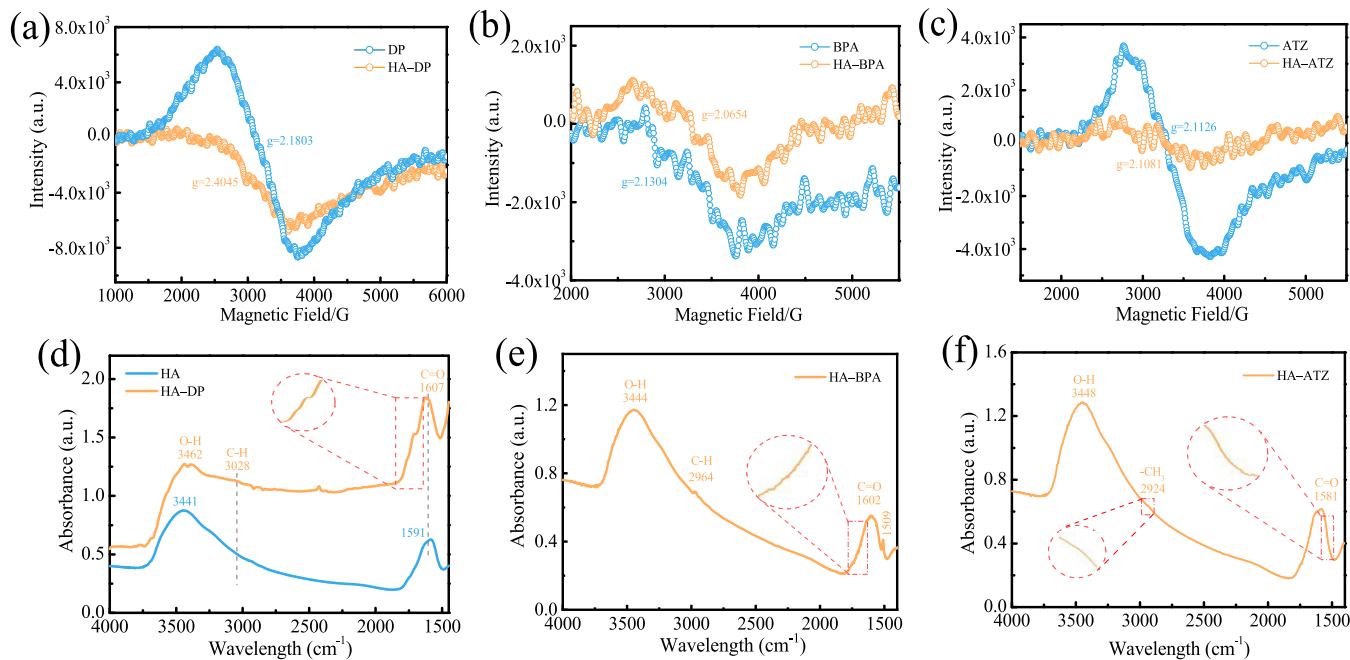


Figure 3. EPR spectra of (a) DP and HA–DP, (b) BPA and HA–BPA, and (c) ATZ and HA–ATZ. FTIR spectra of (d) HA and HA–DP, (e) HA–BPA, and (f) HA–ATZ. Reaction conditions: initial micropollutant concentration 3.0 mg/L, initial HA concentration 10.0 mg/L, and temperature 35 °C.

$\text{Fe}^0\text{-Fe}_y\text{C}_z/\text{Fe}_x\text{-GZIF-8-rGO}$ suspension were identified by GC-MS analysis, including benzyl alcohol, benzaldehyde, phenol, ethylene glycol, hydroacrylic acid, acetic acid, glycerol, nonanoic acid, and some alkanes (Figure S3a,b and Table S1), which was consistent with the direct cleavage and hydrolysis hydroxylation process of DP over $\text{Fe}^0\text{-Fe}_y\text{C}_z/\text{Fe}_x\text{-GZIF-8-rGO}$ according to our previous research.²⁰ Moreover, the above byproducts were quite different from the byproducts (aromatic compounds, long-chain alkanes, and small alcohols) obtained from the destruction of HA in the $\text{Fe}^0\text{-Fe}_y\text{C}_z/\text{Fe}_x\text{-GZIF-8-rGO}/\text{HA}$ suspension (Figure S3c,d and Table S2). The results further confirmed that the tested micropollutants were removed preferentially in water containing HA/DOC through the surface reaction in the $\text{Fe}^0\text{-Fe}_y\text{C}_z/\text{Fe}_x\text{-GZIF-8-rGO}$ suspension.

Electrostatic Coupling of Micropollutants and HA/DOC. DP, BPA, and ATZ as typical structure representatives were selected to investigate the interaction with HA/DOC in water. The characteristic fluorescence peak (peak A) for HA (Figure S4a) significantly enhanced or decreased after interaction with DP, BPA, and ATZ for 30 min (Figure S4b-d), while the characteristic peaks (peak B: aromatic proteins; peak C: tryptophan-like organics; peak D: fulvic acid-like; peak E: humic acid-like)²² for DP, BPA, and ATZ disappeared after the reaction (Figure S5), confirming the formation of the HA–micropollutant complex. After adding DP, BPA, and ATZ, the fluorescence peak intensity for municipal wastewater decreased (Figure S6a-d) more than those of HA–micropollutant samples (Figure S4). The same phenomenon was also observed in the raw drinking water sample with DP, BPA, and ATZ (Figure S7). The results indicated the stronger interaction between micropollutants and DOC in real water. The EPR spectrum of HA showed an obvious EPR signal at $g = 2.0043$ attributable to the semiquinone radical (Figure S8a).²³ Differently, DOC in municipal wastewater and raw drinking water showed a new

EPR signal at $g = 2.1586$ and 2.1773, respectively (Figure S8b,c), which were attributed to single electrons of the complex from DOC aggregation in aquatic systems.¹⁹ The results indicated that the complex formed in municipal wastewater or raw drinking water had a greater electron polarity than pure HA, promoting its interaction with micropollutants.

Furthermore, new EPR signals at $g = 2.4045$, 2.0654, and 2.1081 emerged for HA–DP, HA–BPA, and HA–ATZ samples, respectively, which was ascribed to the single electron (Figure 3a-c).²⁴ However, the EPR signals for HA, DP, BPA, and ATZ disappeared, indicating the conversion of the semiquinone radical and the rapid electron transfer between HA and micropollutants, which confirm their π -conjugated complexes. Expectedly, EPR signals at $g = 2.1903$ and 2.2532 for DOC (municipal wastewater/raw drinking water)–BPA (Figure S9a) and at $g = 2.1714$ and 2.1623 for DOC (municipal wastewater/raw drinking water)–DP (Figure S9b) were observed, which was different from the individual one, indicating the complexation between DOC and micropollutants. Meanwhile, in the FTIR spectra of these samples (Figure 3d-f), HA exhibits adsorption bands representing the benzoquinone group and the phenolic –OH group at 1591 and 3441 cm⁻¹, respectively.^{25,26} The new adsorption bands at 3028 and 2964 cm⁻¹ in HA–DP and HA–BPA were assigned to the C–H stretching in the aromatic ring (Figure 3d,e), while the adsorption band at 2924 cm⁻¹ in HA–ATZ was assigned to the –CH₃ group of ATZ (Figure 3f).²⁷ The results indicated the successful complexation between DP/BPA/ATZ and HA. Additionally, the benzoquinone group shifted to 1607, 1602, and 1581 cm⁻¹ in the corresponding sample, respectively (Figure 3d-f). The new vibration peaks at 1642–1850 cm⁻¹ for HA–DP and at 1633–1760 cm⁻¹ for HA–BPA could be ascribed to the stretching of monosubstituted benzene, and the vibration peaks at 1507–1558 cm⁻¹ for HA–ATZ could be attributed the stretching of N=C–N of

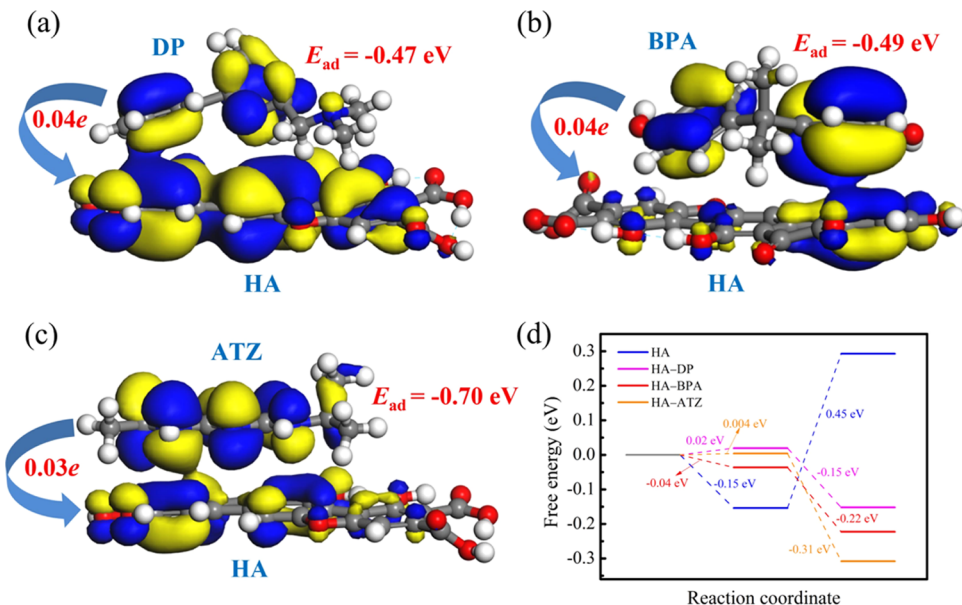


Figure 4. Highest occupied molecular orbital (HOMO) for (a) DP, (b) BPA, and (c) ATZ on the HA model fragments with an isovalue of $0.015\text{ b}^{-3/2}$. (d) Free energy diagrams of the reduction process of the benzoquinone group of HA on various systems.

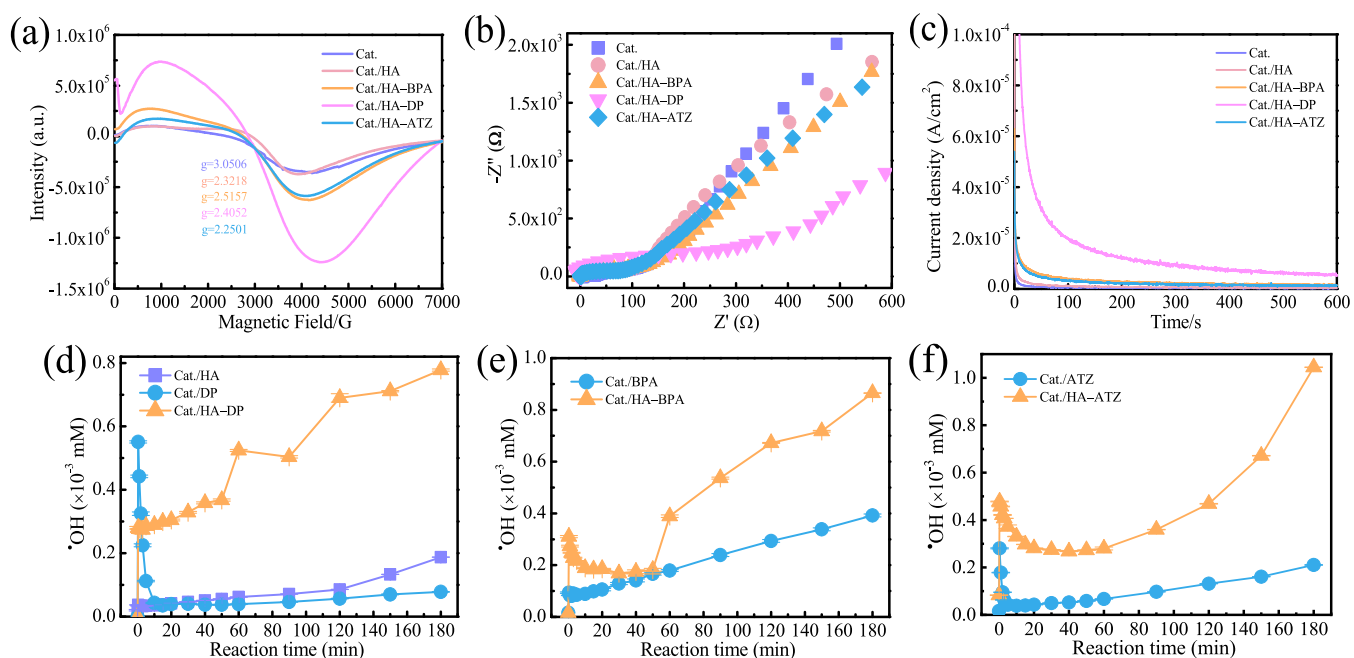


Figure 5. (a) Solid EPR spectra of various samples. (b) EIS and (c) chronoamperometry curves of various samples. Quantitative detection of $\cdot\text{OH}$ in (d) Cat./HA, Cat./DP, and Cat./HA-DP; (e) Cat./BPA and Cat./HA-BPA; and (f) Cat./ATZ and Cat./HA-ATZ air-saturated aqueous suspensions using the terephthalic acid (TPA) probe method. Reaction conditions: catalyst concentration 0.6 g/L, initial micropollutant concentration 3.0 mg/L, initial HA concentration 10.0 mg/L, and temperature 35 °C.

ATZ.²⁸ Notably, the phenolic $-\text{OH}$ group in three complex samples showed a red shift and a higher adsorption intensity than HA. The above results confirmed that the complex was formed through $\pi-\pi$ interaction of the aromatic structure of HA with the aromatic structure of DP, BPA, or ATZ, which caused more electrons to lean toward the carbonyl group in the benzoquinone of HA, producing more electron-rich phenolic $-\text{OH}$ groups in the complex. Therefore, it could be inferred that an electron-poor area appeared on the aromatic structure of DP, BPA, or ATZ. The conjectures were defined using DFT calculations. Figure 4a–c shows that DP, BPA, and ATZ could

complex with HA by $\pi-\pi$ electrostatic forces between their aromatic structure and HAs, with adsorption energies of -0.47 , -0.49 , and -0.70 eV, respectively. Notably, the total atomic charge of HA is 0 e , and it changed to -0.04 , -0.04 , and -0.03 e after DP, BPA, and ATZ adsorbed, respectively, confirming the electron transfer from the aromatic structures of DP, BPA, and ATZ to that of HA in the complex. Therefore, the EPR signals for the single electron could be attributed to the electron-rich phenolic group of HA in the complex, in agreement with the literature.²⁹ Simultaneously, the electron-poor area was formed around the aromatic structures of DP,

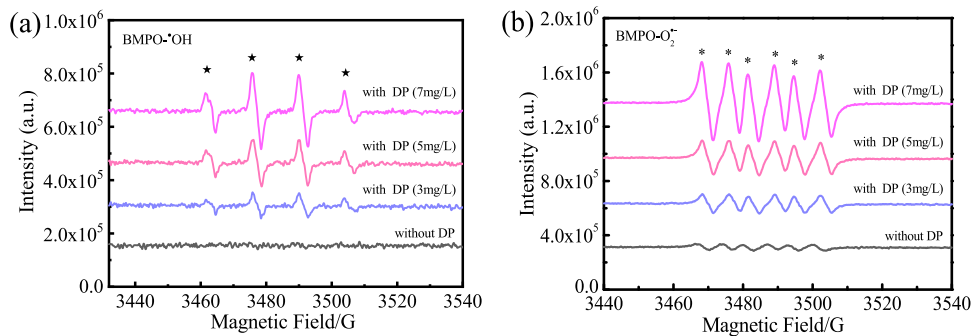


Figure 6. BMPO spin-trapping EPR spectra for (a) $\cdot\text{OH}$ and (b) $\text{O}_2^{\bullet-}$ with/without DP in the $\text{Fe}^0\text{-Fe}_y\text{C}_z/\text{Fe}_x\text{-GZIF-8-rGO/HA}$ air-saturated aqueous suspensions.

BPA, and ATZ of the complex. The reduction of the benzoquinone group of HA to the phenolic group can be divided into two steps: the benzoquinone group of HA was reduced to form the intermediate first (step I) and then was further reduced to form the final product of the phenolic group (step II) (Figure S10). Based on DFT calculations, it was found that step II was the rate-determining step during the reaction, with a ΔG value of 0.45 eV (Figure 4d). However, the rate-determining step changes to the first step when DP, BPA, and ATZ adsorbed on HA with a very small ΔG value (no larger than 0.004 eV). The above results indicated that the formed polar HA–DP/BPA/ATZ complex can promote the reduction process of benzoquinone groups of HA by utilizing electrons from DP/BPA/ATZ of the complex, which could be the fundamental reason for the preferential removal of DP/BPA/ATZ on the $\text{Fe}^0\text{-Fe}_y\text{C}_z/\text{Fe}_x\text{-GZIF-8-rGO}$ surface.

Interfacial Interaction of the HA/DOC–DP/BPA/ATZ Complex and $\text{Fe}^0\text{-Fe}_y\text{C}_z/\text{Fe}_x\text{-GZIF-8-rGO}$. According to a previous study²⁰ and the above results, the HA–DP/BPA/ATZ complex could be adsorbed on the surface of $\text{Fe}^0\text{-Fe}_y\text{C}_z/\text{Fe}_x\text{-GZIF-8-rGO}$ through its benzoquinone group and the phenolic group of HA by the π – π interaction or H-bonding interaction. Figure 5a shows the EPR spectra of the $\text{Fe}^0\text{-Fe}_y\text{C}_z/\text{Fe}_x\text{-GZIF-8-rGO}$ samples before and after reaction with HA–DP/BPA/ATZ in the air-saturated aqueous suspension. $\text{Fe}^0\text{-Fe}_y\text{C}_z/\text{Fe}_x\text{-GZIF-8-rGO}$ showed that the weak EPR signal at $g = 3.0506$ was ascribed to a single electron around the iron species. After adsorbing HA, this EPR signal intensity slightly increased, indicating the interaction of HA and the catalyst. However, for the adsorbed-HA–DP/BPA/ATZ $\text{Fe}^0\text{-Fe}_y\text{C}_z/\text{Fe}_x\text{-GZIF-8-rGO}$ samples, this EPR signal intensity greatly increased and shifted to lower g values (2.4052, 2.5157, and 2.2501) compared to $\text{Fe}^0\text{-Fe}_y\text{C}_z/\text{Fe}_x\text{-GZIF-8-rGO}$, indicating that more electrons were delocalized to the catalyst surface from the adsorbed complex, which should belong to DP/BPA/ATZ according to the above results. Moreover, the electron transfer process was further confirmed using electrochemical methods. Figure 5b shows the electrochemical impedance spectroscopy (EIS) curves of various samples. The pristine $\text{Fe}^0\text{-Fe}_y\text{C}_z/\text{Fe}_x\text{-GZIF-8-rGO}$ showed the biggest arc diameter. After reaction with HA, this arc diameter showed a slight decrease, indicating the decrease in the electron transfer resistance during the reaction. However, for the adsorbed-HA–DP/BPA/ATZ $\text{Fe}^0\text{-Fe}_y\text{C}_z/\text{Fe}_x\text{-GZIF-8-rGO}$ samples, smaller arc diameters were observed, in which the adsorbed-HA–DP $\text{Fe}^0\text{-Fe}_y\text{C}_z/\text{Fe}_x\text{-GZIF-8-rGO}$ sample showed the smallest arc diameter, indicating the lowest electron transfer resistance. Meanwhile, the current density for the corresponding samples

showed the opposite change pattern during the reaction (Figure 5c), which was consistent with the EPR determination. The results confirmed that the adsorbed polarized HA–DP/BPA/ATZ complex could donate more electrons to the electron-rich area around the Fe species of $\text{Fe}^0\text{-Fe}_y\text{C}_z/\text{Fe}_x\text{-GZIF-8-rGO}$ compared with the single compound. Expectedly, stronger single-electron EPR signals appeared on the surface of the adsorbed-DOC–BPA catalyst from municipal wastewater and raw drinking water (Figure S11). The results indicated that more electrons of micropollutants are transferred to the surface of the catalyst by the complex in real water, resulting in the higher elimination of micropollutants in both municipal wastewater and raw drinking water.²⁰

According to a previous work,²⁰ in a reaction system with degradation of micropollutants, hydroxyl radicals ($\cdot\text{OH}$) could be produced due to their surface cleavage and hydrolysis process. Therefore, the generated $\cdot\text{OH}$ was quantitatively analyzed in the $\text{Fe}^0\text{-Fe}_y\text{C}_z/\text{Fe}_x\text{-GZIF-8-rGO}$ air-saturated aqueous suspension with different micropollutants using the terephthalic acid (TPA) probe method (Figure 5d–f). Only 1.8×10^{-4} , 8×10^{-5} , 3.9×10^{-4} , and 2.1×10^{-4} mM $\cdot\text{OH}$ were produced within 180 min during HA–DP/BPA/ATZ degradation. For HA–DP/BPA/ATZ complex degradation, the amount of the produced $\cdot\text{OH}$ increased slowly within 60 min due to incomplete complexation between the HA and the pollutant. Then, it promptly increased and approximately 7.8×10^{-4} , 8.7×10^{-4} , and 1.04×10^{-3} mM $\cdot\text{OH}$ were produced at 180 min, much higher than the individual one. Meanwhile, the EPR spin-trapping technique with BMPO was also used to determine the generated $\cdot\text{OH}$ and $\text{O}_2^{\bullet-}$ during HA–DP complex degradation under otherwise identical conditions (Figure 6). In the absence of DP, a weak BMPO– $\cdot\text{OH}$ EPR signal appeared in the $\text{Fe}^0\text{-Fe}_y\text{C}_z/\text{Fe}_x\text{-GZIF-8-rGO/HA}$ suspension (Figure 6a). In the presence of DP, this EPR signal gradually enhanced on increasing the DP concentration from 3 to 7 mg/L. Correspondingly, the BMPO– $\text{O}_2^{\bullet-}$ EPR signals increased with increasing DP concentration (Figure 6b). Also, the same phenomenon was observed in HA–BPA/ATZ suspensions (Figure S12). The results indicated that the DP/BPA/ATZ of the adsorbed-HA–DP/BPA/ATZ complexes was responsible for both $\cdot\text{OH}$ and $\text{O}_2^{\bullet-}$ generation. As indicated by solid EPR and FTIR analyses and DFT calculations, there is an electron-rich area around the phenolic group of HA and an electron-poor area around the aromatic structure of DP/BPA/ATZ on the HA–DP/BPA/ATZ complex. Based on a previous work,²⁰ the electron-rich area was around the iron species and the electron-poor area was around the aromatic rings of GZIF-8 and rGO on the surface

of $\text{Fe}^0\text{-Fe}_y\text{C}_z/\text{Fe}_x\text{-GZIF-8-rGO}$. Therefore, the complexes were able to adsorb on the electron-poor area of the catalyst through the phenolic group of HA and delocalized electrons of DP/BPA/ATZ to electron-rich iron species area; then, these electrons were trapped by dissolved O_2 to form $\text{O}_2^{\bullet-}$. Moreover, more electron-poor areas formed around the aromatic structure of DP/BPA/ATZ of the adsorbed complex due to the $\pi-\pi$ interaction between them and HA, causing their hydroxylation and cleavage by the strong surface electrostatic force and ensuring pollutant destruction preferentially. During the reaction, the HA and DOC in ultrapure water, municipal wastewater, and raw drinking water played complexation and electron shuttle roles.

■ ASSOCIATED CONTENT

SI Supporting Information

The Supporting Information is available free of charge at <https://pubs.acs.org/doi/10.1021/acs.est.2c03354>.

Supporting experimental details; ESP distribution for different structural model fragments; structures of various micropollutants; GC-MS chromatograms of various samples; 3D-EEM fluorescence spectroscopy of different samples; solid EPR spectra of various samples; reduction steps of benzoquinone groups of the HA fragment to phenolic groups through DFT calculations; EPR spectra for BMPO- $\bullet\text{OH}$ and BMPO- $\text{O}_2^{\bullet-}$ in various suspensions; and main products during the catalytic degradation process of HA-DP and HA (Tables S1 and S2) ([PDF](#))

■ AUTHOR INFORMATION

Corresponding Author

Chun Hu — Institute of Environmental Research at Greater Bay, Key Laboratory for Water Quality and Conservation of the Pearl River Delta, Ministry of Education, Guangzhou University, Guangzhou 510006, China;  orcid.org/0000-0003-3217-7671; Phone: +86-20-39346609; Email: huchun@gzhu.edu.cn

Authors

Yumeng Wang — Institute of Environmental Research at Greater Bay, Key Laboratory for Water Quality and Conservation of the Pearl River Delta, Ministry of Education, Guangzhou University, Guangzhou 510006, China

Peng Zhang — Institute of Environmental Research at Greater Bay, Key Laboratory for Water Quality and Conservation of the Pearl River Delta, Ministry of Education, Guangzhou University, Guangzhou 510006, China

Lai Lyu — Institute of Environmental Research at Greater Bay, Key Laboratory for Water Quality and Conservation of the Pearl River Delta, Ministry of Education, Guangzhou University, Guangzhou 510006, China;  orcid.org/0000-0002-5624-961X

Tong Li — Institute of Environmental Research at Greater Bay, Key Laboratory for Water Quality and Conservation of the Pearl River Delta, Ministry of Education, Guangzhou University, Guangzhou 510006, China;  orcid.org/0000-0003-2508-8339

Complete contact information is available at: <https://pubs.acs.org/10.1021/acs.est.2c03354>

Notes

The authors declare no competing financial interest.

■ ACKNOWLEDGMENTS

This work was supported by the National Natural Science Foundation of China (52150056, 51838005) and the introduced innovative R&D team project under the "The Pearl River Talent Recruitment Program" of Guangdong Province (2019ZT08L387).

■ REFERENCES

- (1) Schwarzenbach, R. P.; Escher, B. I.; Fenner, K.; Hofstetter, T. B.; Johnson, C. A.; von Gunten, U.; Wehrli, B. The challenge of micropollutants in aquatic systems. *Science* **2006**, *313*, 1072.
- (2) Yang, T.; Mai, J.; Cheng, H.; Zhu, M.; Wu, S.; Tang, L.; Liang, P.; Jia, J.; Ma, J. UVA-LED-assisted activation of the Ferrate(VI) process for enhanced micropollutant degradation: Important role of Ferrate(IV) and Ferrate(V). *Environ. Sci. Technol.* **2022**, *56*, 1221–1232.
- (3) Fenner, K.; Canonica, S.; Wackett, L. P.; Elsner, M. Evaluating pesticide degradation in the environment: Blind spots and emerging opportunities. *Science* **2013**, *341*, 752–758.
- (4) Aguas, Y.; Hincapie, M.; Martínez-Piernas, A. B.; Agüera, A.; Fernández-Ibáñez, P.; Nahim-Granados, S.; Polo-López, M. I. Reclamation of real urban wastewater using solar advanced oxidation processes: An assessment of microbial pathogens and 74 organic microcontaminants uptake in lettuce and radish. *Environ. Sci. Technol.* **2019**, *53*, 9705–9714.
- (5) Jans, U.; Prasse, C.; Gunten, U. Enhanced treatment of municipal wastewater effluents by FeTAML/ H_2O_2 : Efficiency of micropollutant abatement. *Environ. Sci. Technol.* **2021**, *55*, 3313–3321.
- (6) Kümmerer, K.; Dionysiou, D. D.; Olsson, O.; Fatta-Kassino, D. A path to clean water. *Science* **2018**, *361*, 222–224.
- (7) Rizzo, L.; Malato, S.; Antakyalı, D.; Beretsou, V. G.; Đolić, M. B.; Gernjak, W.; Heath, E.; Ivancev-Tumbas, I.; Karaolia, P.; Ribeiro, A. R. L.; Mascolo, G.; Mc Ardell, C. S.; Schaar, H.; Silva, A. M. T.; Fatta-Kassinos, D. Consolidated vs new advanced treatment methods for the removal of contaminants of emerging concern from urban wastewater. *Sci. Total Environ.* **2019**, *655*, 986–1008.
- (8) Tran, N. H.; Reinhard, M.; Gin, K. Y. H. Occurrence and fate of emerging contaminants in municipal wastewater treatment plants from different geographical regions—a review. *Water Res.* **2018**, *133*, 182–207.
- (9) Li, M.; Hao, M.; Yang, L.; Yao, H.; Bolton, J. R.; Blatchley, E. R., III; Qiang, Z. Trace organic pollutant removal by VUV/UV/chlorine process: Feasibility investigation for drinking water treatment on a mini-fluidic VUV/UV photoreaction system and a pilot photoreactor. *Environ. Sci. Technol.* **2018**, *52*, 7426–7433.
- (10) Shi, J. L.; Plata, S. L.; Kleimans, M.; Childress, A. E.; McCurry, D. L. Formation and fate of nitromethane in ozone-based water reuse processes. *Environ. Sci. Technol.* **2021**, *55*, 6281–6289.
- (11) Li, M.; Li, W.; Bolton, J. R.; Blatchley, E. R.; Qiang, Z. Organic pollutant degradation in water by the vacuum-ultraviolet/ultraviolet/ H_2O_2 process: Inhibition and enhancement roles of H_2O_2 . *Environ. Sci. Technol.* **2019**, *53*, 912–918.
- (12) Lee, Y.; Gerrity, D.; Lee, M.; Bogaat, A. E.; Salhi, E.; Gamage, S.; Trenholm, R. A.; Wert, E. C.; Snyder, S. A.; von Gunten, U. Prediction of micropollutant elimination during ozonation of municipal wastewater effluents: use of kinetic and water specific information. *Environ. Sci. Technol.* **2013**, *47*, 5872–5881.
- (13) Yang, T.; Mai, J.; Cheng, H.; Zhu, M.; Wu, S.; Tang, L.; Liang, P.; Jia, J.; Ma, J. UVA-LED-assisted activation of the Ferrate(VI) process for enhanced micropollutant degradation: Important role of Ferrate(IV) and Ferrate(V). *Environ. Sci. Technol.* **2022**, *56*, 1221–1232.
- (14) Wang, J.; Fu, Q.; Yu, J.; Yang, H.; Hao, Z.; Zhu, F.; Ouyang, G. An ultrafast and facile nondestructive strategy to convert various

- inefficient commercial nanocarbons to highly active Fenton-like catalysts. *Proc. Natl. Acad. Sci. U.S.A.* **2022**, *119*, No. e2114138119.
- (15) Pei, D. N.; Liu, C.; Zhang, A. Y.; Pan, X. Q.; Yu, H. Q. In situ organic Fenton-like catalysis triggered by anodic polymeric intermediates for electrochemical water purification. *Proc. Natl. Acad. Sci. U.S.A.* **2020**, *117*, 30966–30972.
- (16) Hodges, B. C.; Cates, E. L.; Kim, J. H. Challenges and prospects of advanced oxidation water treatment processes using catalytic nanomaterials. *Nat. Nanotechnol.* **2018**, *13*, 642–650.
- (17) Kim, C.; Chin, Y. P.; Son, H.; Hwang, I. Activation of persulfate by humic substances: Stoichiometry and changes in the optical properties of the humic substances. *Water Res.* **2022**, *212*, No. 118107.
- (18) Nie, J.; Zou, J.; Yan, S.; Song, W. Photosensitized transformation of peroxymonosulfate in dissolved organic matter solutions under simulated solar irradiation. *Environ. Sci. Technol.* **2022**, *56*, 1963–1972.
- (19) Kerner, M.; Hohenberg, H.; Ertl, S.; Reckermann, M.; Spitz, A. Self-organization of dissolved organic matter to micelle-like microparticles in river water. *Nature* **2003**, *422*, 150–154.
- (20) Wang, Y.; Lyu, L.; Wang, D.; Yu, H. Q.; Li, T.; Gao, Y.; Li, F.; Crittenden, J. C.; Zhang, L.; Hu, C. Cation- π induced surface cleavage of organic pollutants with $\cdot\text{OH}$ formation from H_2O for water treatment. *iScience* **2021**, *8*, No. 102874.
- (21) Dougherty, D. A. Cation- π interactions in chemistry and biology: A new view of benzene, phe, tyr, and trp. *Science* **1996**, *271*, 163–168.
- (22) Chen, W.; Westerhoff, P.; Leenheer, J. A.; Booksh, K. Fluorescence excitation-emission matrix regional integration to quantify spectra for dissolved organic matter. *Environ. Sci. Technol.* **2003**, *37*, 5701–5710.
- (23) Witwicki, M.; Jerzykiewicz, M.; Jaszewski, A. R.; Jezierska, J.; Ozarowski, A. Influence of Pb(II) ions on the EPR properties of the semiquinone radicals of Humic acids and model compounds: High field EPR and relativistic DFT studies. *J. Phys. Chem. A* **2009**, *113*, 14115–14122.
- (24) Gao, Y.; Zhu, Y.; Lyu, L.; Zeng, Q.; Xing, X.; Hu, C. Electronic structure modulation of graphitic carbon nitride by oxygen doping for enhanced catalytic degradation of organic pollutants through peroxymonosulfate activation. *Environ. Sci. Technol.* **2018**, *52*, 14371–14380.
- (25) Tohry, A.; Dehghan, R.; Zarei, M.; Chelgani, C. Mechanism of humic acid adsorption as a flotation separation depressant on the complex silicates and hematite. *Miner. Eng.* **2021**, *162*, No. 106736.
- (26) Hu, S.; Jin, X.; Yang, C.; Wang, Y.; Xie, X.; Zhang, S.; Jin, P.; Wang, X. C. Enhanced complexation of humic acids: Homogenization of protonated groups in the hybrid ozonation-coagulation process. *Chemosphere* **2021**, *280*, No. 130647.
- (27) Deng, S.; Bai, R. B. Aminated Polyacrylonitrile Fibers for Humic Acid Adsorption: Behaviors and Mechanisms. *Environ. Sci. Technol.* **2003**, *37*, 5799–5805.
- (28) Jiang, X.; He, W., Eds. Infrared Spectroscopy of Spectrum Recognition Method. *Concise Identification of Infrared Spectroscopy Method*; Guangxi Normal University Press: Guilin, 1992.
- (29) Aeschbacher, M.; Graf, C.; Schwarzenbach, R. P.; Sander, M. Antioxidant Properties of Humic Substances. *Environ. Sci. Technol.* **2012**, *46*, 4916–4925.

□ Recommended by ACS

Degradation of Microplastics by a Thermal Fenton Reaction

Kunsheng Hu, Shaobin Wang, et al.

NOVEMBER 24, 2021
ACS ES&T ENGINEERING

READ ▾

Sustainable Removal of Microplastics and Natural Organic Matter from Water by Coagulation–Flocculation with Protein Amyloid Fibrils

Mohammad Peydayesh, Raffaele Mezzenga, et al.
JUNE 25, 2021
ENVIRONMENTAL SCIENCE & TECHNOLOGY

READ ▾

Mixed-Matrix Membrane Adsorbers for the Simultaneous Removal of Different Pharmaceutical Micropollutants from Water

Sarah Uebel, Thomas Schiestel, et al.
FEBRUARY 16, 2022
ACS APPLIED POLYMER MATERIALS

READ ▾

Porous Cellulose Acetate/Block Copolymer Membranes for the Recovery of Polyphenolic Compounds from Aquatic Environments

José L. Ramírez-Colón, Eduardo Nicolau, et al.
JANUARY 11, 2022
ACS OMEGA

READ ▾

Get More Suggestions >